Extending the Atmospheric Radiative Transfer Simulator (ARTS) to Shortwave Radiation

JAMES | Journal of Advances in Modeling Earth Systems

RESEARCH ARTICLE
10.1029/2025MS005024

Extending the Atmospheric Radiative Transfer Simulator (ARTS) to Shortwave Radiation

Manfred Brath[1], Jon Petersen[1,2], Stefan A. Buehler[1], and Patrick Eriksson[3]

[1]Center for Earth System Research and Sustainability (CEN), Meteorological Institute, University of Hamburg, Hamburg, Germany, [2]Now at Sunnic Lighthouse GmbH, Hamburg, Germany, [3]Department of Space, Earth and Environment, Chalmers University of Technology, Gothenburg, Sweden

Key Points:

- Atmospheric Radiative Transfer Simulator (ARTS) is extended to the shortwave radiation
- This allows consistent all sky radiative transfer simulations from the microwave to the ultraviolet

Correspondence to:
M. Brath,
manfred.brath@uni-hamburg.de

Citation:
Brath, M., Petersen, J., Buehler, S. A., & Eriksson, P. (2026). Extending the Atmospheric Radiative Transfer Simulator (ARTS) to shortwave radiation. *Journal of Advances in Modeling Earth Systems*, *18*, e2025MS005024. https://doi.org/10.1029/2025MS005024

Received 19 FEB 2025
Accepted 3 MAR 2026

Author Contributions:
Conceptualization: Manfred Brath, Jon Petersen, Stefan A. Buehler, Patrick Eriksson
Formal analysis: Manfred Brath, Jon Petersen
Investigation: Manfred Brath, Jon Petersen
Methodology: Manfred Brath, Jon Petersen
Software: Manfred Brath, Jon Petersen
Supervision: Stefan A. Buehler, Patrick Eriksson
Validation: Manfred Brath, Jon Petersen
Visualization: Manfred Brath
Writing – original draft: Manfred Brath, Jon Petersen
Writing – review & editing: Manfred Brath, Stefan A. Buehler, Patrick Eriksson

Abstract Atmospheric Radiative Transfer Simulator (ARTS) is an open source general purpose radiative transfer model used for a wide range of applications from remote sensing to the interaction of climate and radiation. In the past, it was confined to the microwave and infrared spectral range, as ARTS could not simulate the interaction of solar radiation in the atmosphere. Here we close this gap and extend ARTS to the shortwave range. We introduce a solar source that can be used as a collimated beam source and as background source allowing to resolve the finite solar disc. Additionally, we implemented a new clear sky solver that supports collimated beam sources and solar background sources, and updated the ARTS DISORT interface to utilize DISORT's capability for collimated beam sources. This allows consistent line-by-line radiative transfer simulations from the microwave to the ultraviolet range with ARTS. We evaluated the shortwave capabilities of ARTS by comparing it with LBLRTM for clear sky simulations. The root mean square deviation between them is 0.70 Wm^{-2} for the upward flux at top of the atmosphere and 0.66 Wm^{-2} for the downward flux at the surface. Simulations of a sunrise as seen from space, of satellite observations and of full spectrum all sky radiative flux illustrate the new capabilities. With the new features, ARTS can be used for a wide range of new applications.

Plain Language Summary The Atmospheric Radiative Transfer Simulator (ARTS) is an open source model to simulate how radiation, like sunlight, infrared and microwaves, are absorbed, scattered, and emitted by gases, clouds, and particles in the air. Originally, ARTS could only work with certain types of radiation, specifically in the microwave and infrared ranges, it couldn't simulate sunlight. In this study, we improved ARTS to handle sunlight as well, known as shortwave radiation. Now, ARTS can simulate light across a broader range, from microwaves to infrared and even ultraviolet light. We tested the new sunlight features of ARTS by comparing its results with another model for clear sky conditions, and we found that they matched closely. We demonstrated what the improved ARTS can do by simulating natural color satellite images, a sunrise seen from space, and the full spectrum of all sky radiation.

1. Introduction

The interaction of electromagnetic (EM) radiation with the atmosphere is the foundation for atmospheric remote sensing and the driving force of the climate system. Radiative transfer models help to understand and exploit this interaction. Atmospheric Radiative Transfer Simulator (ARTS) is an open source general purpose radiative transfer model used for a multitude of applications ranging from remote sensing to the interaction of climate and radiation (Buehler et al., 2005, 2018, 2025; Eriksson et al., 2011). As ARTS so far could not simulate highly directed sources, it could not simulate solar radiation observations or solar radiation energy fluxes. It was limited to thermal radiation or in the context of terrestrial temperatures it was limited to microwave (MW) and infrared (IR) radiation, though the actual line-by-line calculation of ARTS was already used for simualting absorption cross section in the shortwave range (Emde et al., 2016; Gasteiger et al., 2014). We extend ARTS to the shortwave range by introducing a collimated beam source (CBS), incorporating molecular scattering and updating the surface handling. The new features are part of the latest version of ARTS (2.6). A general description of ARTS 2.6 is given by Buehler et al. (2025). These new features allow consistent radiative transfer simulations from the MW to the UV range of the EM spectrum. So, there is no longer the necessity to combine ARTS with another model when simulating the whole EM spectrum as previously done for example, by Kluft et al. (2021). They used a combination of ARTS and RRTMG (Rapid Radiative Transfer Model for GCMs (Mlawer et al., 1997)) for their radiative convective equilibrium simulations where ARTS and RRTMG were used for longwave and shortwave radiation, respectively. With ARTS now capable of simulating shortwave, it can be used for longwave and

shortwave reducing inconsistencies due to the different model assumptions and types. The goal of this article is to describe the new shortwave features of ARTS and illustrate their capabilities but also their limitations in the context of clear sky and all sky simulations.

The article is structured as follows. The next section gives an overview about ARTS. Section 3 explains and describes the new ARTS features. Section 4 illustrates the new features in the context of clear sky simulations and evaluate ARTS shortwave capabilities by comparing it with LBLRTM (S. Clough et al., 2005) and other radiative transfer models from Pincus et al. (2020). Section 5 illustrates the new features in the context of all sky simulations and Section 6 concludes the article.

2. ARTS General Overview

In this section we give a short overview about ARTS. Further details on the latest version and the history of ARTS are given by Buehler et al. (2025). Previous versions are described by Buehler et al. (2018), Eriksson et al. (2011) and Buehler et al. (2005). ARTS is a general purpose atmospheric radiative transfer model. The ability to define observation geometries, sensor characteristics and calculate Jacobian (weighting functions) makes it a powerful tool for remote sensing retrievals. It has also a dedicated interface for optimal estimation method retrievals. Absorption is handled by line-by-line calculations, continua models and absorption cross-section spectra. ARTS comes with its own line and cross-section catalog. The line catalog is based on the high-resolution transmission molecular absorption database (HITRAN, (Gordon et al., 2022)) as of 2022–05–02. The cross-section catalog was derived from HITRAN absorption cross-section data using the arts-crossfit-package (Buehler et al., 2022). The arts-crossfit-package can be used to convert absorption cross-section data from different sources to ARTS internal format.

Internally ARTS uses spectral radiance, expressed in $\mathrm{Wm}^{-2}\ \mathrm{sr}^{-1}\ \mathrm{Hz}^{-1}$, as radiation quantity or the corresponding Stokes vector for polarized radiative transfer. ARTS also provides functions to convert between different radiance units, such as per wavelength or wavenumber or even brightness temperature. ARTS computes spectral radiance for any user-defined set of frequencies, such as the frequency grids described in Sections 4 and 5.2, without limitations on the number of frequencies. For each frequency, ARTS performs radiative transfer calculations, including the determination of absorption coefficients. When calculating the absorption coefficients by line-by-line, all spectral line data that have an impact on the absorption at that frequency are considered.

ARTS assumes in general an ellipsoidal atmosphere, but it can also handle plane parallel atmospheres.

The atmosphere can be 1D, 2D or 3D. This means, atmospheric variables like temperature, pressure, density, etc. vary only in the vertical dimension (1D), have no longitude variation (2D) or vary in altitude, latitude and longitude (3D). Polarization is fully described by using the Stokes formalism. ARTS has two internal scattering solvers (DOIT, MC) and has interfaces to two 3rd party scattering solvers namely PolRadTran's RT4 solver (Evans & Stephens, 1995) and CDISORT (Buras et al., 2011), which is a port of DISORT 2.1 (Stamnes et al., 2000) to C.

ARTS internal solvers can account for refraction. However, in this article refraction is not considered, as ARTS currently lacks a refractive index parametrization for the shortwave range.

ARTS is written in C++ and has a Python interface. This allows the user to control ARTS and to conduct simulations using Python. For macOS and Linux precompiled binaries are available, which can be installed in a Miniforge (https://github.com/conda-forge/miniforge) environment with the mamba package manager. Miniforge is an installer for conda and mamba pre-configured to use conda-forge, which is used to install ARTS and its dependencies. To install ARTS with mamba use the following command: `mamba install rttools::pyarts`.

This will install the latest release version, which is currently ARTS 2.6.16. For archiving purposes, there is also a package of the exact version used in this article on Zenodo (Buehler et al., 2024) The absorption catalog (arts-cat-data) and additional data (arts-xml-data) like atmospheric profiles, solar spectra, scattering data can be downloaded for the corresponding ARTS version with the Python command `pyarts.cat.download.retrieve()` or from the ARTS homepage (https://www.radiativetransfer.org/).

We also provide an additional python package (pyarts-fluxes) for simulating radiative fluxes with ARTS available from GitHub (https://github.com/atmtools/pyarts-fluxes). It is an easy-to-use wrapper to simulate radiative fluxes with ARTS. The idea of the wrapper is to prepare a basic setup so that users can calculate radiative fluxes with ARTS in a straight forward manner without having to deal with all the details of an ARTS simulation setup but still have full control over the simulation setup. If needed, the users can modify it as they like. The package also include some examples to get started. The wrapper is explicitly designed to be used in combination with the ARTS Python interface. The wrapper does not work without it. This wrapper was also used to simulate the clear sky fluxes in Section 4.1 and can be also used to simulate the fluxes like in Section 5.2. Note that with the next release, ARTS 3, this functionality will move into the pyarts core package.

3. Implementation of Solar Radiation

This section is about the implementation of solar radiation. First, we describe how ARTS simulates solar radiation. Second, we describe how it is incorporated into simulations. Finally, we describe the additional features which were further needed.

The simulation of solar radiation in ARTS is based on the assumption that the distance between the sun and the top of the atmosphere (TOA) of the planet d_{sun} is much larger than the radius r_{sun} of the sun.

$$r_{sun} \ll d_{sun}. \tag{1}$$

This means that the angular variability of the direction of the radiation from the sun can be neglected and is assumed to be parallel (collimated beam approximation, (Stamnes et al., 2017)). In that case, the incoming spectral radiance at TOA at solid angle Ω can be described as

$$I_{sun,\mathrm{TOA}}(\Omega) = F_{sun,\mathrm{TOA}}\delta(\Omega - \Omega') \tag{2}$$

with Ω' the solid angle from the sun to the TOA and $F_{sun,\mathrm{TOA}}$ the incoming spectral flux (spectral irradiance) from the sun at TOA. In this article we use the term spectral flux and spectral irradiance interchangeably. For an ellipsoidal atmosphere as used in ARTS, $F_{sun,\mathrm{TOA}}$ depends on the geographical position, because the distance between the sun and the TOA varies for different positions on the planet. For example, the distance between the sun and Earth's TOA is about 6,400 km smaller at the equator than at the poles. The resulting difference is small, in the order of 0.1 Wm^{-2}, but it can be important for reference simulations especially when comparing to simulation with other geometries. This implementation enables ARTS to simulate different distances to the sun and different radii without requiring additional modifications.

The spectral flux of the incoming radiation from the sun at TOA $F_{sun,\mathrm{TOA}}$ is

$$\begin{aligned} F_{sun,\mathrm{TOA}} &= \int_0^{2\pi}\int_0^{\alpha} I_{sun}\cos\theta\sin\theta \mathrm{d}\theta\mathrm{d}\phi \\ &= \pi I_{sun}\sin^2\alpha \\ &= F_{sun}\sin^2\alpha, \end{aligned} \tag{3}$$

with α the angular radius of the sun, I_{sun} the hemispherically isotropic radiance leaving the surface of the Sun, F_{sun} the spectral radiation flux at the position of the sun in space. F_{sun} describes the radiation properties of the sun, see Section 3.2. The factor $\sin^2\alpha$ takes into account that the irradiance is changing with the inverse square of the distance as it is

$$\sin^2\alpha = \frac{r_{sun}^2}{d_{sun,\mathrm{TOA}}^2 + r_{sun}^2} \tag{4}$$

with $d_{sun,\mathrm{TOA}}$ the distance between the sun and the TOA of the planet. The angular radius of the sun seen from TOA of the planet is α,

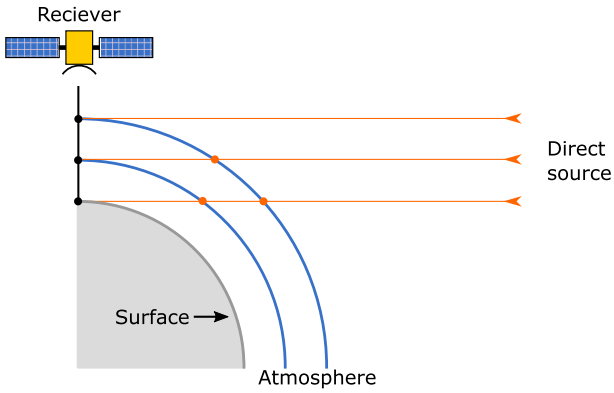

Figure 1. Sketch of the geometry of the iyClearsky-solver.

$$\alpha = \arcsin\sqrt{\frac{r_{sun}^2}{d_{sun}^2 + r_{sun}^2}} = \arctan\frac{r_{sun}}{d_{sun}}. \tag{5}$$

3.1. Simulations With Solar Radiation

There are two ways to conduct simulations with solar radiation:

1. ARTS internal clear sky solver iyClearsky or
2. CDISORT (Buras et al., 2011), which is DISORT 2.1 (Stamnes et al., 2000) ported to C.

ARTS internal scattering solvers (DOIT, MC) are not suitable for solar radiation simulations, as they do not support collimated beam sources and are limited to thermal radiation only.

3.1.1. iyClearsky

iyClearsky is one of ARTS' internal clear sky solvers. In this context clear sky means that there is no scattering by cloud or aerosol particulates but only scattering and absorption by molecules. It assumes a 3D atmosphere, can handle polarization and can use multiple solar sources. It includes only single scattering of the direct solar beam as the atmospheric scattering source. Multiple scattering and scattering of thermal emission are ignored. At the surface, both the diffuse field and the direct solar beam contribute to scattering, but the upward scattered radiation is not fed back as a source for subsequent scattering in the atmosphere.

With this the radiative transfer equation can be approximated for the unpolarized case as

$$\frac{\mathrm{d}I}{\mathrm{d}s} = -kI + aB(T) + \sigma\sum_{n=1}^{N_{suns}} F_{sun,n}^{*}\, P(\Omega', \Omega_s) \tag{6}$$

with I the spectral radiance, s the position along the propagation path (black ray in Figure 1), k, a, σ the extinction, absorption and scattering coefficient, B the Planck function, Ω' the incoming and Ω_s the direction of the propagation path, P the normalized phase function and N_{suns} the number of solar sources (in the case of Earth only one). All quantities on the right-hand side in Equation 6 except for Ω' and Ω_s are functions of ν and s.

The propagation path describe the path of the radiation. As ARTS does not include a refractive index parametrization for the shortwave so far, the propagation paths in this article are always straight lines.

The incoming direct radiation $F_{sun,n}^{*}$ of solar source n at along track position s is

$$F_{sun,n}^{*}(\nu, s) = F_{sun,\mathrm{TOA}}(\nu, s)\,\exp\left(-\int_{s}^{s_{toa}} k(\nu, s')\,\mathrm{d}s'\right) \tag{7}$$

with s' the position along the path from the position s to TOA in the direction of the sun (orange rays in Figure 1) and $F_{sun,\mathrm{TOA}}$ the incoming radiation flux from the sun at TOA. We omit the polarized case here for simplicity, but it is implemented in ARTS.

Equation 6 is solved for any desired line of sight direction using a first order integration scheme, see also Section 2.1 in Buehler et al. (2025). Depending on the viewing direction the surface of the planet, space or the surface of the sun is used as background source. By using the sun also as background source the actual geometry is considered as shown in Section 4.2, while as source term the sun is treated as a point source. Therefore, the radiance of the sun "surface" is used as background radiance, which is assuming an isotropic spectral radiance

$$I_{sun} = \frac{F_{sun}}{\pi}. \tag{8}$$

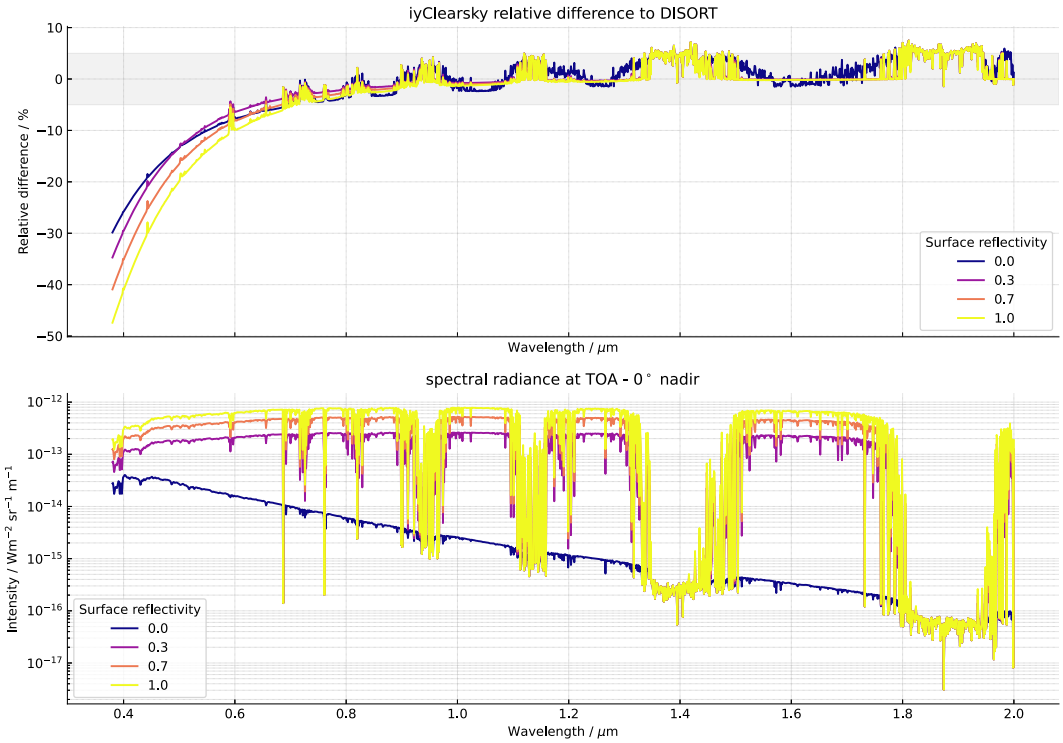

Figure 2. Comparison of the upward radiation at top of the atmosphere (TOA) from iyClearsky and DISORT for a tropical atmosphere for different surface reflectivities. The solar zenith angle is 0° and the viewing angle is 0° nadir (looking straight down) (top) Relative difference between iyClearsky and DISORT (bottom) Spectral radiance at TOA from DISORT.

The background source defines the start of the propagation path. The simulated sensor can be inside the atmosphere, at the surface or in space. As ARTS assumes an ellipsoidal atmosphere Equation 6 is also solved for limb viewing geometries, see Section 4.2 for an example. While iyClearsky's limitations restrict its range of applications, it provides a foundation for further development of ARTS' shortwave capabilities. As the simplest solver for a scattering atmosphere, iyClearsky already incorporates spherical atmospheric geometry, polarization, collimated beam sources, and a solar background source, which allows to simulate the finite solar disc.

3.1.2. Limitations of iyClearsky

By neglecting multiple scattering and the scattering contribution from the surface upwelling, iyClearsky is confined to cases with low surface reflectivity and small single scattering albedo. Getting an error estimate for the approximation of iyClearsky is not straight forward because it depends on the viewing geometry, the solar zenith angle, the surface reflectivity, the wavelength and the atmospheric composition.

Figure 2 shows the relative difference between iyClearsky and DISORT at TOA for a tropical atmosphere, considering various surface reflectivities with the sun at zenith and looking straight down (0° nadir). The simulation setup is similar to that described in Section 4.1. Neglecting multiple scattering leads to an underestimation at TOA of approximately 25% at 0.4 μm for a non-reflecting surface, increasing to about 42% for a fully reflecting surface. As surface reflectivity increases, the difference becomes larger due to enhanced multiple scattering from surface upwelling. At 0.6 μm, the underestimation is around 7% for a non-reflecting surface and 10% for a fully reflecting surface. For wavelengths above 0.7 μm, differences remain within ±5% regardless of surface reflectivity, reflecting the diminished impact of Rayleigh scattering.

The overestimation of radiance by iyClearsky beyond 1.0 μm arises from differences in how iyClearsky and DISORT solve the radiative transfer equation. Because Rayleigh scattering is weak at these wavelengths, multiple scattering is not important. iyClearsky solves the radiative transfer equation using a first order scheme to integrate the radiative transfer equation along the line of sight, whereas DISORT employs a discrete-ordinate method that solves the entire radiation field. Furthermore, iyClearsky assumes that atmospheric properties vary linearly

between grid points, while DISORT uses a layer model with constant properties within each layer. When absorption changes strongly over a short distance from small to large values—this can lead to differences between the solvers at these wavelengths. For example, at 1.38 μm (a water vapor absorption band), water vapor varies strongly with altitude in the lower troposphere, leading to large absorption gradients. At wavelengths where absorption is weak, the differences between the two solvers are practically zero. These differences can be mitigated by increasing the number of atmospheric grid points in the simulation, so that the assumptions about the atmospheric profile become more similar.

With increasing solar zenith angles and more oblique viewing directions, the underestimation grows due to longer atmospheric path lengths.

For limb-viewing geometries, we cannot make a similar comparison with CDISORT, as it does not support limb configurations. Oikarinen et al. (1999) investigated the impact of multiple scattering in limb-viewing geometry. Although their scenario differs from ours because they also included aerosol scattering, their results give a good estimate of the order of magnitude of the multiple-scattering contribution in limb-viewing geometry. The multiple-scattering contribution depends on the angle between the solar direction and the viewing direction. In the direction of the Sun, the multiple-scattering contribution is about 5% for a wavelength of 500 nm, increases as the angle between the Sun and the viewing direction approaches 90°, and decreases again for larger angles. When the Sun is directly above the tangent point, the multiple-scattering contribution is about 50%, and when the Sun is located roughly 90° to the side of the line of sight and close to or below the horizon, the signal is almost entirely due to multiple scattering. In the case of pure molecular scattering, the multiple-scattering contribution is smaller because, due to the less forward-peaked phase function, the probability that single-scattered light reaches the sensor is higher.

Neglecting the scattering contribution from the surface upwelling results in an underestimation of the upward radiation at TOA of approximately 10% at 0.4 μm wavelength and of approximately 5% or less for wavelengths >0.55 μm for a surface reflectivity of 0.3 if the sun is at zenith and looking straight down. With increasing solar zenith angles the underestimation decreases because the surface scattering is proportional to the cosine of the solar zenith angle and because of the increased extinction by the increased path length through the atmosphere. On the other hand, for oblique viewing angles the underestimation increases due to the increased path. For limb-viewing directions, the light reflected by the surface constitutes about 20% of the total signal for a surface reflectivity of 0.3 when the sun is directly above the tangent point, and roughly 40% if the surface reflectivity is 1. With increasing solar zenith angle, this contribution decreases Oikarinen et al. (1999).

With increasing wavelength the error decreases because the scattering cross-section decreases and Rayleigh scattering becomes weaker.

3.1.3. CDISORT

CDISORT is a port of DISORT 2.1 (Stamnes et al., 2000) to C by Buras et al. (2011). It is integrated in ARTS as a 3rd party solver. This section gives a short overview of the solver, see Stamnes et al. (2000) and Buras et al. (2011) for more details. DISORT is well established and used in many radiative transfer models for example, libRadtran (Emde et al., 2016) or MODTRAN (Berk & Hawes, 2017). It is known to be very accurate and fast. From here on CDISORT is called DISORT for the sake of simplicity.

DISORT is a 1D radiative transfer solver for unpolarized radiation and can handle multiple scattering. It assumes plane parallel atmospheres without refraction and can have one solar source. Within ARTS DISORT can handle molecular scattering and particulate scattering. In this article we consider only hydrometeors (clouds) for particulate scattering. We exclude aerosols because we did not provide any scattering data for aerosols so far as we do for hydrometoers like the scattering database of Yang et al. (2013) and Bi and Yang (2017) in the ARTS single scattering data format, which is freely available from Zenodo (https://doi.org/10.5281/zenodo.10807525. However, aerosols can be included if the user provides the scattering data in the ARTS single scattering data format and describe the particle size distribution using a modified gamma distribution.

Apart from simulating the radiances, DISORT has also a dedicated mode to simulate irradiances, which makes it ideal for the simulation of radiation fluxes, which avoids the need to integrate radiance over solid angle.

As DISORT is a plane parallel solver and ARTS assumes an ellipsoidal atmosphere, it needs to be run for a specific geographic position because the local solar zenith angle, which DISORT internally needs, is calculated from this geographic position and the geographic zenith position of the sun. Furthermore, the incoming solar radiation at TOA is calculated specifically for this geographic position.

The coupling of DISORT with ARTS depends on the specific application. Typically, DISORT is integrated via a cloudbox mechanism in ARTS. In this approach, ARTS prepares all necessary input parameters for DISORT—such as single scattering albedo, phase function, temperature, and optical depth—and then invokes DISORT to compute spectral radiances throughout the atmosphere. The results from DISORT are applied only within the user-defined cloudbox, which extends from the surface up to a specified upper boundary. Above this boundary, ARTS uses its internal clearsky solvers for radiative transfer calculations. e.g., if a sensor is above the cloudbox, ARTS uses the radiance at the upper boundary of the cloudbox as background radiance for the internal clear sky solvers. This means, that line-of-sight integration toward the sensor starts at the upper boundary of the cloudbox. If the sensor is within the cloud box, ARTS interpolates the DISORT results to the sensor position and view direction. In this article, we set the upper boundary always to the TOA. For the simulation of fluxes, DISORT is always used for the full atmosphere.

3.2. Sun

This section briefly describes how we implemented and designed a sun in ARTS. Generally, there can be multiple suns in ARTS each with their individual irradiance spectra. ARTS assumes that the spectrum is given at the position of the sun. This gives flexibility for simulations with multiple suns or different positions of the sun. The input radiation at TOA $F_{sun,\mathrm{TOA}}$ over a specific geographical position is directly calculated from the angular diameter of the sun α as seen from that position and the irradiance spectrum F_{sun} at the position of the sun in space (Equation 5). In addition to the spectrum of the sun, the radius and distance must be given by the user. Defaults for this are reference values of our Sun ($r_{sun} = 6.96342 \cdot 10^8$ m) and the astronomical unit as the distance $R_{sun} = 1\mathrm{au} = 1.495978707 \cdot 10^{11}$ m. The sun can be placed anywhere in the sky. It is specified by the geographical location at which the sun is at zenith. Though not realistic for Earth, but if desired the sun could be at zenith at the North Pole.

A solar spectrum can be defined by a black body with an effective emission temperature or with an arbitrary user-defined spectrum. In case of an arbitrary user-defined spectrum, the effective temperature is used to extrapolate the spectrum for frequencies outside the range of the user-defined spectrum. By setting the effective temperature to zero the spectrum is confined to the user-defined spectrum. For frequencies within the user-defined spectrum, the spectrum is linearly interpolated onto the simulation spectral grid. The arts-xml-data package contains five preprocessed solar spectra based on the reference spectra from NOAA's Solar Spectral Irradiance (SSI) Climate Data Record (CDR) (Coddington et al., 2017). Additional solar spectral data can be downloaded for example, from NOAA (https://www.ncei.noaa.gov/products/climate-data-records/solar-spectral-irradiance, 13 February 2025).

3.3. Molecular Scattering

The Rayleigh scattering cross-section $\sigma_{\mathrm{Ray,xsec}}$ is calculated using a parametrization from M. Callan, University of Colorado Stamnes et al. (2017) who fitted the scattering cross section of Bates (1984).

$$\sigma_{\mathrm{Ray,xsec}}(\lambda) = \lambda^{-4} \sum_{i=0}^{3} a_i \lambda^{-2i} \cdot 10^{-28} \left[\mathrm{cm}^2\right] \tag{9}$$

with $a_0 = 3.9729066$, $a_1 = 4.6547659 \cdot 10^{-2}$, $a_2 = 4.5055995 \cdot 10^{-4}$, and $a_3 = 2.3229848 \cdot 10^{-5}$. This parametrization is limited to Earth and accurate to 0.3% for wavelengths between 0.205 and 1.05 μm. Rayleigh scattering cross-section models like the actual one from Bates (1984), from Bodhaine et al. (1999) or Tomasi et al. (2005) will be added in the future. The actual Rayleigh scattering coefficient assuming ideal gas law is

$$\sigma_{\mathrm{Ray}} = N \sigma_{\mathrm{Ray,xsec}} = \frac{p}{T k_b} \sigma_{\mathrm{Ray,xsec}} \tag{10}$$

with N the number density, p the pressure, T the temperature and k_b the Boltzmann constant.

The Rayleigh phase matrix (Hansen & Travis, 1974) including depolarization is

$$\mathbf{P} = \frac{3}{4}\Delta \begin{pmatrix} 1+\cos^2\Theta & -\sin^2\Theta & 0 & 0 \\ -\sin^2\Theta & 1+\cos^2\Theta & 0 & 0 \\ 0 & 0 & 2\cos\Theta & 0 \\ 0 & 0 & 0 & \Delta' 2\cos\Theta \end{pmatrix} + (1-\Delta) \begin{pmatrix} 1 & 0 & 0 & 0 \\ 0 & 0 & 0 & 0 \\ 0 & 0 & 0 & 0 \\ 0 & 0 & 0 & 0 \end{pmatrix} \tag{11}$$

with Θ the scattering angle and

$$\Delta = \frac{1-\rho}{1+\frac{\rho}{2}} \tag{12}$$

$$\Delta' = \frac{1-2\rho}{1-\rho} \tag{13}$$

and ρ the depolarization factor. Measured values for ρ are given by Penndorf (1957). By default ρ is set to 0.03, which is the value for air, but it can be set to any user defined value. The depolarization factor depends in general on the wavelength and can be calculated from the King factor (Eberhard, 2010). In the future, when Rayleigh scattering cross-section models for example, like the one from Bates (1984) will be available, the depolarization factor will be calculated from the King factor for the corresponding wavelength.

3.4. Surfaces

Depending on the solver, different surfaces can be used. The iyClearsky solver can be used with Lambertian surfaces or specular surfaces when using CBS. Whereas in iyClearsky the molecular scattering is only driven by CBS, the surface scattering is driven by CBS and the diffuse radiation. A specular surface can be used with a fixed reflectivity or with reflectivity according to the Fresnel equations. There are more for surfaces types in ARTS, but they are not supported with a CBS. Within ARTS DISORT can handle only Lambertian surfaces. DISORT itself can handle also bidirectional reflectance distribution functions (Buras et al., 2011) but this is not implemented in ARTS yet. Further surface types like a wind roughened ocean surface will be added in the future.

4. Clearsky Simulations

This section focuses on clear sky simulations in the visible spectral range. First, we show the simulation of clear sky shortwave fluxes for the present day scenario from the Radiative Forcing Model Intercomparison Project (RFMIP (Pincus et al., 2016)) and compare them with fluxes simulated with LBLRTM v12.8 (S. Clough et al., 2005) from Pincus et al. (2020). This serves also as validation, because it tests ARTS' capability to simulate absorption in the shortwave range. In the context of this article, flux means the radiative flux, see also Appendix A for the definition. Second, we show the simulation of a sunset as seen from space, which summarizes the capabilities and the limitations of the iyClearsky solver.

4.1. Clear Sky Shortwave Fluxes

Within RFMIP, atmospheric conditions for 100 different sites are given for 18 different experiments. The experiments represent conditions in different epochs or climate scenarios. For this work, only the "present-day" experiment was used. For all sites, latitude and longitude, surface temperature, emissivity, and albedo, as well as the total solar irradiance (TSI) and solar zenith angle, are given. Temperature and pressure are given on 61 vertical levels. For these levels, the fluxes are simulated. The atmospheric composition is defined for the layers between these levels, where only water vapor and ozone change with height. Gas absorption was taken into account by using the ARTS line by line catalog, which is based on the HITRAN (Gordon et al., 2022) database, MT_CKD for continuum absorption version 3.5 for H_2O and version 2.5.2 for CO_2 (Mlawer et al., 2012), collision-induced absorption from MT_CKD version 1.0 for O_2 (Thibault et al., 1997) and version 2.5.2 for N_2 (Lafferty

Table 1
List of Considered RFMIP Species for the Flux Simulations in Section 4.1. O_3 is Treated for Wavelengths >1.4 μm as Line-By-Line Species and for Wavelengths Shorter Than That as Absorption Cross-Section Species

Line-by-line	O_2, N_2, H_2O, O_3, CH_4, CO, CO_2, CH_3Br, CH_3Cl, N_2O
Absorption cross-sections	NF_3, SF_6, SO_2F_2, CH_2Clv, CH_3CCl_4, HCFC141
	HCFC142, CFC113, CFC114, CFC115, CFC11, CFC12
	Halon1211, Halon1301, Halon2402, CCl_4, CF_4
	C_iF_{2i+2} with $i \in \{2,3,4,5,6,8\}$
	HCFC22, HFC125, HFC134, HFC143, HFC152, HFC227
	HFC23, HFC32, HFC4310
	O_3

et al., 1996) and the ARTS cross-section catalog. For the line-by-line calculation a cutoff of 750 GHz (Paynter & Ramaswamy, 2011) is used. Molecular scattering was taken into account by using the Rayleigh phase matrix and the Rayleigh cross-section from Section 3.3. The main absorption species within the shortwave range are water vapor, ozone, oxygen and carbon dioxide. Table 1 lists all absorption species used in the simulations. Most of these species apart from the main absorbers will only slightly impact the shortwave fluxes, but we left them in the simulation setup for consistency.

As the aim is to evaluate the shortwave fluxes, Planck emission is excluded. For the angular resolution, 10 streams (discrete ordinates in DISORT) are used. This means for every hemisphere 5 streams are used. The fluxes were simulated with DISORT using 32768 equidistantly sampled wavelengths from 115.5 nm to 9,999.5 nm, which corresponds to a spectral resolution (sampling interval) of 0.3 nm. Tests with a four times higher spectral resolution showed that the fluxes are within 0.1%. Even with a much coarser grid of approximately 10,000 wavelengths, the fluxes differed by only 0.6%. At first glance, a spectral resolution of 0.3 nm or even 0.075 nm might appear too coarse for accurate flux calculations, since not all spectral line features are resolved. However, as demonstrated below, a 0.3 nm resolution yields sufficiently accurate fluxes. The reason for that is that due to high density of spectral lines, an equidistant spectral grid leads to a quasi-random sampling of the spectral lines features. This causes positive and negative errors to largely cancel out (Buehler et al., 2006). Although Buehler et al. (2006) focused on longwave radiation, the same reasoning applies to the shortwave range. Thus, it is crucial to capture the overall spectral variability, rather than resolve every individual line feature.

RFMIP implicitly assumes a plane parallel atmosphere in its scenarios as they specify the solar incoming radiation only by the TSI at TOA and the solar zenith angle at TOA. Within RFMIP the TSI varies between sites to account for the different distances between the Sun and the Earth due to Earth's elliptical orbit. The distance is 0.9832899 au in the perihelion and 1.0167103 au in the aphelion, which are the closest and farthest points, respectively. The difference in distance can cause a difference of 6.93% in flux at the TOA. Though the plane parallel assumption is often sufficient, it is not completely realistic as it neglects the curvature of the Earth and its atmosphere. ARTS takes account of the curvature as it assumes ellipsoidal atmosphere. In an ellipsoidal atmosphere the incoming radiation at TOA depends on the geographical position (see Section 3) and cannot simply be specified with TSI and solar zenith angle. Therefore, we have to adjust the solar source for each site to match the TSI at TOA of the simulation site.

The sun is modeled using the SSI CDR reference spectrum of May 2004 (Coddington et al., 2017) rescaled for every site to match the TSI at TOA of each site. Effectively, this means within ARTS that we have to create for each site a new solar source. Within ARTS the position of the sun is not defined by the solar zenith angle but where the sun is at zenith. To mimic the RFMIP solar zenith angle, the zenith position of the sun is set along the equator toward the east at the longitude φ that matches the solar zenith angle θ.

$$\varphi = \theta - \arcsin\left(\frac{R_{earth}}{R_{sun}}\sin(\pi - \theta)\right) \tag{14}$$

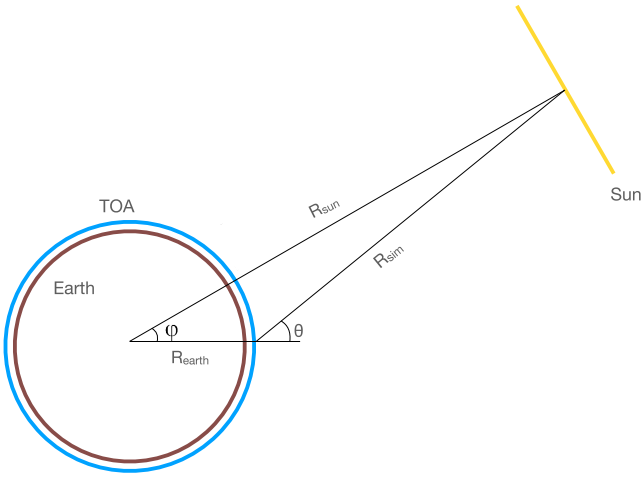

Figure 3. Illustration of the geometry of Earth and Sun in Atmospheric Radiative Transfer Simulator. Shown are angles and distances between the center of the Sun, the center of the Earth and a simulation location. See Section 4.1 for details.

with R_{earth} the TOA altitude seen from the Earth's center and R_{sun} the distance from the Earth's center to the Sun. Using the solar zenith angle θ as longitude results in an error of about 0.1 Wm^{-2} in the flux at TOA, because the solar zenith angle θ is larger than the longitude φ at which the Sun is at zenith (Figure 3).

We want to emphasize that these adjustments are only needed because RFMIP implicitly assumes a plane parallel atmosphere in its scenarios otherwise these adjustments are not needed.

The incoming fluxes at TOA drive all radiation in the shortwave regime. Therefore, it is vital that the incoming fluxes at TOA are accurate. The root mean square deviation (RMSD) between the TSI of LBLRTM from Pincus et al. (2020) and ARTS is 0.004 Wm^{-2} or $6 \cdot 10^{-4}$%.

At the surface the relative difference for the downward between both models is mostly less than 0.5% (Figure 4c). Differences >1% are found at locations where the flux at the surface is small (Figure 4a). At TOA the relative difference for the upward flux is about 0.7% (Figure 4d). Compared to the downward flux at the surface, there is no significant change in the difference if the flux is small (Figure 4b). Figures 4c and 4d also show the relative difference between the SW models from Pincus et al. (2020) and LBLRTM. The other SW models are UK Met Office SOCRATES (Suite Of Community RAdiative Transfer codes based on Edwards and Slingo (Edwards & Slingo, 1996)), GRTCODE a line-by-line code developed at NOAA Geophysical Fluid Dynamics Lab (GFDL), and the Reference Forward Model (RFM (Dudhia, 2017)). UK Met Office provided the results for SOCRATES, which are labeled accordingly to (Pincus et al., 2020) as HadGEM3, and GFDL provided the results for GRTCODE and RFM. From each model and physics variant, we use only one forcing variant because the difference between these variants is negligible. For the downward flux at the surface the difference for ARTS is between the difference of RFM and HadGEM3.

Table 2 summarizes the results from the different models. It contains the bias and RMSD of the downward flux at the surface and of the upward flux at TOA. ARTS has a RMSD of 0.70 Wm^{-2} for the upward flux at TOA and 0.66 Wm^{-2} for the downward flux at the surface. The bias is 0.62 Wm^{-2} for the upward flux at TOA and 0.36 Wm^{-2} for the downward flux at the surface. The bias of the upward flux at TOA is almost as big as the RMSD indicating that there is a systematic difference between ARTS and LBLRTM. For the downward flux the bias is only roughly half of the RMSD. Of the other models only RFM has lower RMSDs with 0.14 Wm^{-2} for the upward flux at TOA and 0.40 Wm^{-2} for the downward flux at the surface.

In summary, ARTS shows good agreement with LBLRTM, with biases and RMSDs comparable to those of other models in Pincus et al. (2020), demonstrating ARTS's capability to simulate shortwave radiation.

4.2. Sunrise From Space

In this subsection, we simulate a sunrise as seen from space for a clear sky atmosphere. Clear sky in the context of this article means that there are no clouds, aerosols or other particulates in the atmosphere. The main purpose of this example is to demonstrate the basic capabilities of the iyClearsky solver. Within its limitations as described in Section 3.1.2, iyClearsky is capable of simulating limb viewing geometries, can handle solar occultation and the curvature of the atmosphere and can resolve the finite solar disc. As ARTS lacks a refractive index parametrization for the shortwave so far, we exclude refraction, though iyClearsky can handle it. Plane parallel solvers like DISORT cannot handle limb viewing geometries. An overview of other radiative transfer models capable of limb viewing geometries can be found in the work of Zawada et al. (2021), where they systematically compared these models. Figure 5a shows the sun as it is risen half above the horizon as seen from space. The simulated sensor is located 25,000 km above the equator at 0° longitude looking eastward toward the sun. The atmospheric conditions are taken from the FASCOD tropical atmosphere (Anderson et al., 1986). Included gases are H_2O, O_2, N_2, O_3, CO_2, N_2O, CO and CH_4. The image was simulated with a spectral resolution of 1 nm from 380 to 2,000 nm. Gas absorption was taken into account by using ARTS' line by line data, which is based on the HITRAN (Gordon et al., 2022) database, MT_CKD for continuum absorption version 3.5 for H_2O and version 2.5.2 for CO_2

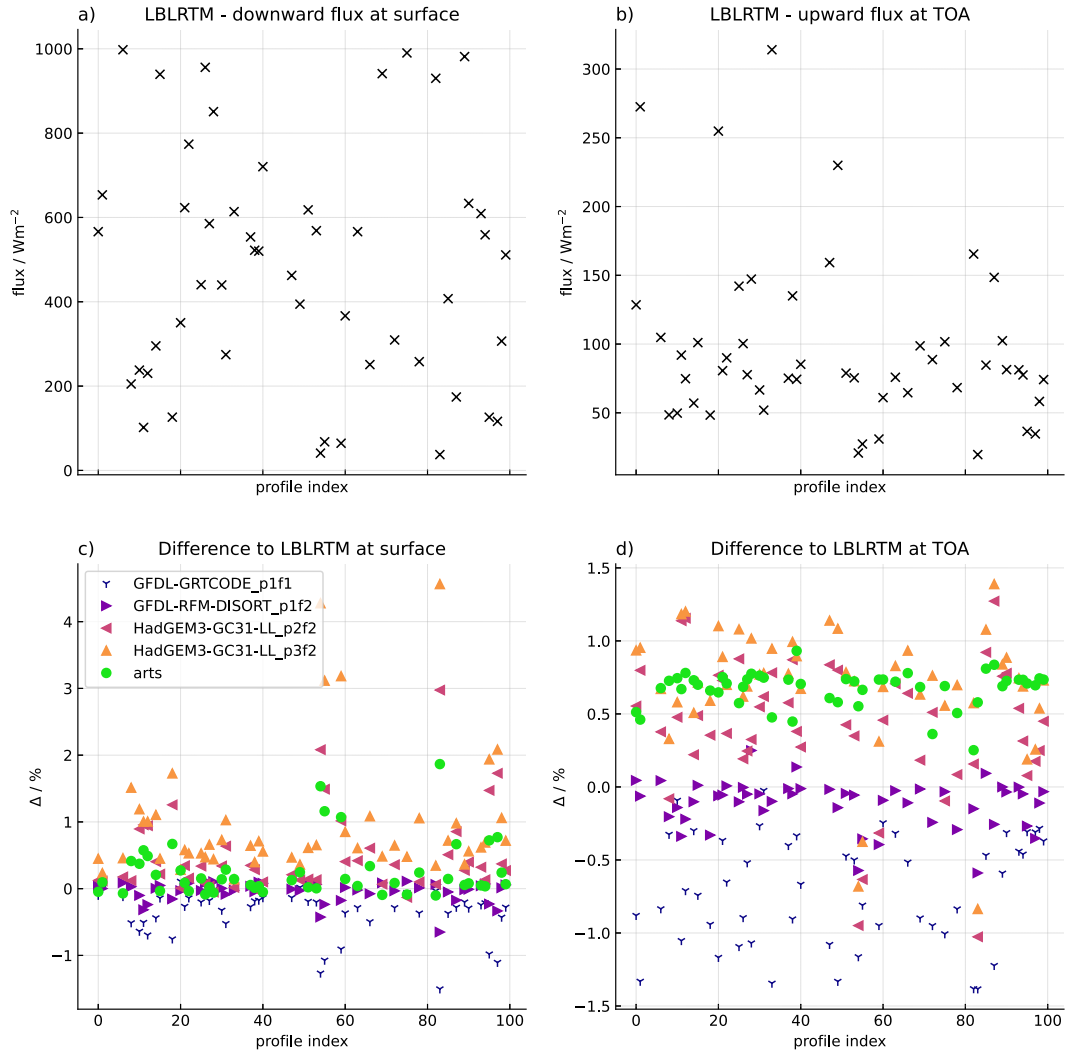

Figure 4. (a) LBLRTM SW downward flux at the surface for RFMIP present day scenario from Pincus et al. (2020). (b) Same as (a) but for upward flux at top of the atmosphere (TOA). (c) Relative differences between SW models from Pincus et al. (2020) and LBLRTM and between Atmospheric Radiative Transfer Simulator and LBLRTM for downward fluxes at the surface. (d) Same as (b) but for upward flux at TOA. See text for details.

Table 2
Bias and Root Mean Square Deviation of the Downward Flux at the Surface and the Upward Flux at Top of the Atmosphere for the Present Day Scenario From RFMIP

Model	Bias_{up} [Wm^{-2}]	Bias_{down} [Wm^{-2}]	RMSD_{up} [Wm^{-2}]	RMSD_{down} [Wm^{-2}]
GFDL-GRTCODE_p1f1	−0.822	−0.976	1.246	1.112
GFDL-RFM-DISORT_p1f2	−0.075	0.106	0.142	0.396
HadGEM3-GC31-LL_p2f2	0.539	1.151	0.819	1.405
HadGEM3-GC31-LL_p3f2	0.809	2.946	1.082	3.108
ARTS	0.617	0.359	0.699	0.661

Note. Biases and RMSDs are calculated between SW models from Pincus et al. (2020) and LBLRTM and between ARTS and LBLRTM.

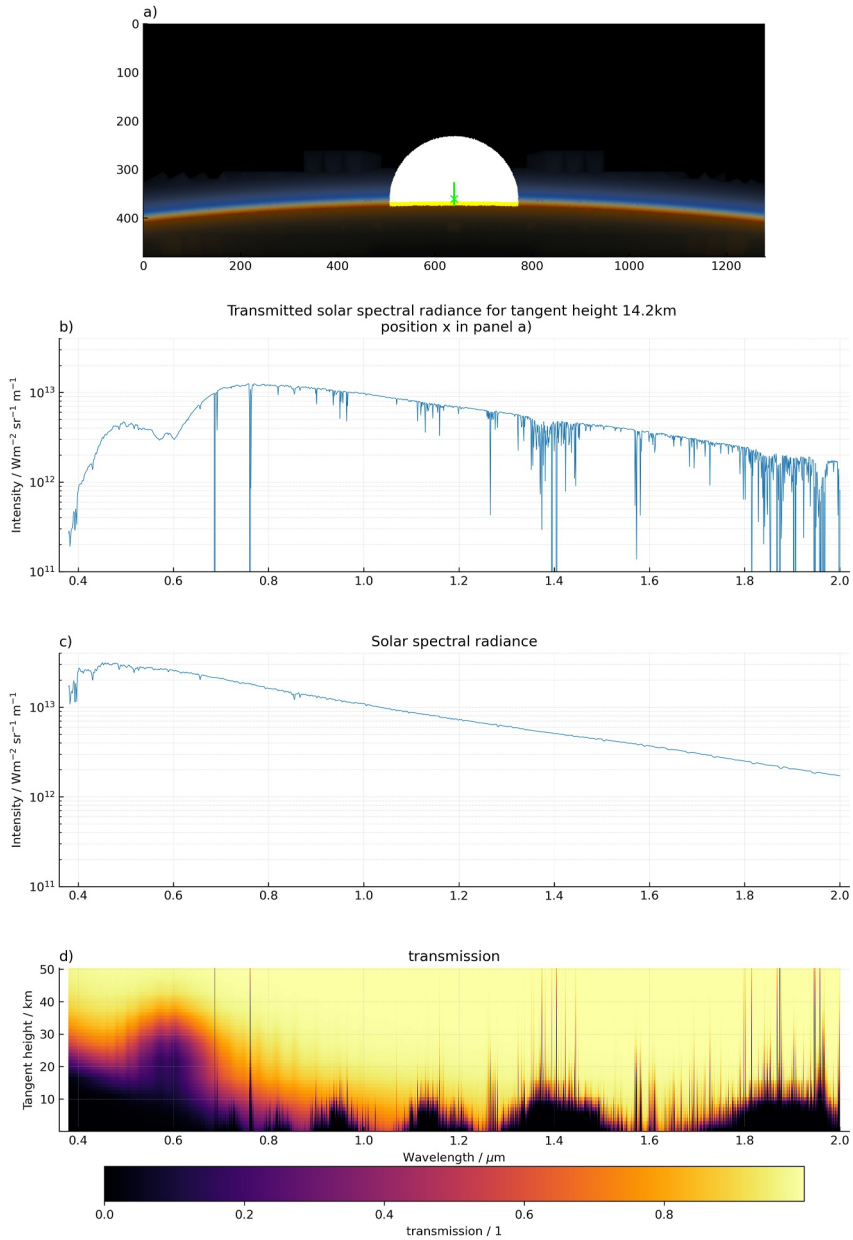

Figure 5. Sunrise from space. (a) Simulated image of a sunrise as seen from space. (b) Transmitted solar spectral radiance. (c) Incoming solar spectral radiance. (d) Transmission $t(\lambda, z_t)$ as function of the tangent height.

(Mlawer et al., 2012), collision-induced absorption from MT_CKD version 1.0 for O_2 (Thibault et al., 1997) and version 2.5.2 for N_2 (Lafferty et al., 1996) and ARTS cross-section catalog for ozone. The ozone cross-section data was derived from Gorshelev et al. (2014) and Serdyuchenko et al. (2014) using the arts-crossfit-package (Buehler et al., 2022). Molecular scattering was taken into account by using the Rayleigh phase matrix and the Rayleigh cross-section defined in Section 3.3. The surface is assumed to be specular with reflectivity according to the Fresnel equations. The spectrum of each pixel is converted to RGB according to Walker (2017). To reduce computing time the simulation was performed for a subset of 30225 pixels and then interpolated to generate the full image.

Figure 5 shows the simulated sunrise as observed from space, covering a horizontal angle of 2.5° and a vertical angle of 0.9375°. The finite extent of roughly half a solar disc (≈0.5° width) and the curvature of the Earth are both clearly depicted. As refraction is excluded in this simulation, the solar disc is undistorted. If refraction were

included, the apparent shape of the solar disc would be distorted. Because the refractive index of air is larger near the surface than at higher altitudes, the light rays from the lower part of the solar disc would be bent more strongly than those from the upper part. Given the viewing geometry, we would expect the entire solar disc to be visible if refraction were included. The apparent shape of the solar disc would change from nearly circular near the upper edge to more elliptical near the lower edge. Not only the Sun would be distorted, but also atmospheric features close to the horizon. Therefore, whenever the precise position of the horizon or the apparent shape and position of the solar disc are of interest, refraction must be included. To illustrate the effect of refraction in a simple way, consider an observer at the surface looking toward the Sun at the horizon. Approximating the atmosphere as an 8 km thick layer with a constant refractive index of 1.0003, the apparent change in the solar zenith angle $\Delta\theta$ due to refraction is

$$\Delta\theta = \arcsin\left(\frac{n_1 R_0}{n_0 R}\right) - \arcsin\left(\frac{R_0}{R}\right) = 0.36^\circ \tag{15}$$

where R_0 is the Earth's radius, R is the Earth's radius plus the atmospheric thickness, $n_0 = 1$ is the refractive index outside the atmosphere, and n_1 is the refractive index within the atmosphere. This means, that the apparent posistion is shifted by rougly 75% of its angular diameter. The sun would appear 0.36° higher than without refraction, making the sun visible even when it is geometrically just below the horizon.

Near the horizon, the color transitions from black through dark blue to lighter blue and yellowish tones, with a dark red band at the bottom, consistent with Rayleigh scattering effects. Since multiple scattering is not included, the simulated colors are darker than expected. Figure 5b displays the transmitted solar spectral radiance spectrum after traversing the atmosphere with a tangent height of 14.2 km (corresponding to the position marked "x" in Figure 5a). The spectrum is shaped not only by Rayleigh scattering but also by molecular absorption, resulting in distinct absorption features such as those from O_2 near 0.69 and 0.76 μm, the dip around 0.6 μm from the Chappuis band of O_3 or the water vapor absorption band around 1.4 μm. The solar spectral radiance spectrum outside of the atmosphere is shown in Figure 5c. It is derived from the SSI CDR reference spectrum of May 2004 (Coddington et al., 2017) that has nominal resolution of 1 nm. The transmission of the solar spectrum varies depending on its path through the atmosphere. This is illustrated in Figure 5d. It shows the transmission t as function of the wavelength λ and the tangent height z_t.

$$t(\lambda, z_t) = \frac{I_{atm}(\lambda, z_t)}{I_{sun}(\lambda)} \tag{16}$$

with I_{atm} the transmitted solar spectral radiance and I_{sun} the solar spectral radiance at TOA. The green line in Figure 5a indicates the tangent height range of Figure 5d. Above 40 km the atmosphere is practically transparent except for the O_2 absorption lines as seen in Figure 5b and some water wapor lines. Between 40 and 16 km the impact of the ozone layer is clearly visible (0.45−0.7 μm) due to the absorption of O_3 in the Chappuis band. Below 20 km the attenuation is mainly due to the Rayleigh scattering for wavelengths <0.7 μm, which is indicated by the smooth decrease of the transmission with increasing wavelength. Above 0.7 μm the transmission is dominated by absorption of water vapor.

5. All Sky Simulations

5.1. All Sky Simulation of Satellite Images

In the past, ARTS could simulate only the longwave channels of sensors like SEVIRI or MODIS. With the new features, ARTS can now simulate the shortwave channels as well. Figure 6 shows simulated images as seen from a geostationary satellite with spectral channels like MODIS (left) and SEVIRI (right). Both images show corrected reflectances R_c

$$R_c = \frac{\pi I_{TOA}}{\mu_0 F_0}, \tag{17}$$

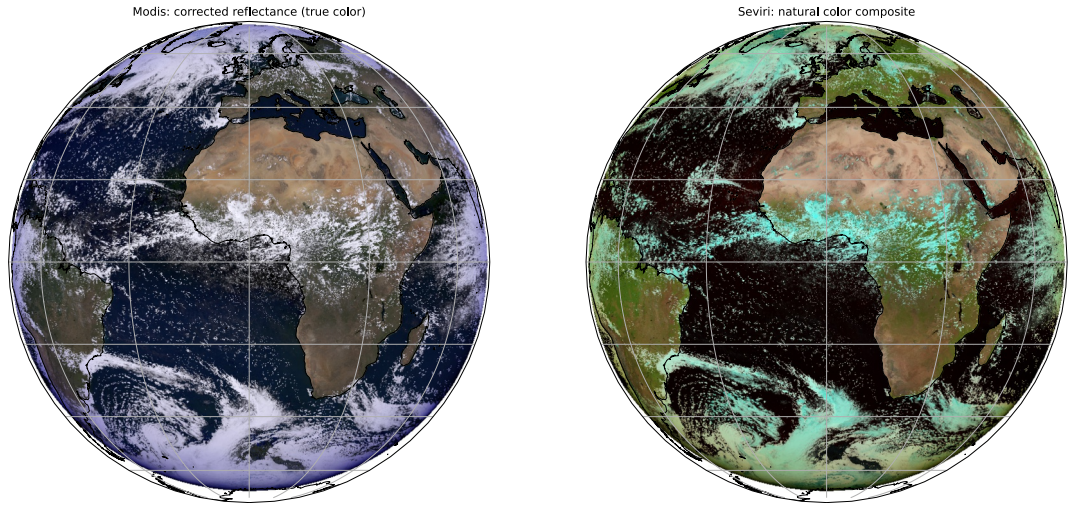

Figure 6. Simulation of geostationary satellite images with spectral channels like MODIS (left) and SEVIRI (right). The images show corrected reflectances R_c of three different spectral channels mapped to RGB. The MODIS image combines three visible channels, resulting in a natural color appearance, whereas the SEVIRI image combines one visible and two near-infrared channels, resulting in a false color appearance. See Table 3 for the channel definitions.

with I_{TOA} the spectral upward radiance at TOA, F_0 the solar irradiance at TOA, and μ_0 the cosine of the solar zenith angle. The reflectances are mapped to RGB channels according to Table 3. MODIS channel 1, 4 and 3 and SEVIRI channels 1 to 3 with one wavelength point per channel were simulated, see Table 3 for the exact wavelengths. The channel definitions were taken from https://space.oscar.wmo.int/instruments/view/seviri (19 September 2024) and https://modis.gsfc.nasa.gov/about/specifications.php (19 September 2024). The RGB mapping for SEVIRI is based on the RGB mapping of the SEVIRI true color product from EUMETSAT (2025). Sensor response functions are supported in ARTS, but they were neglected for this simulation. The simulations were performed separately for each 1D atmospheric profile using the DISORT solver with 16 streams to simulate spectral radiances.

As expected from the channel definitions, the ice clouds appear in blueish colors in the SEVIRI image. This is due to the strong absorption of ice clouds at 1,640 nm (SEVIRI channel 3), resulting in reduced brightness in the red channel, which gives ice clouds a blueish appearance. In contrast, liquid water clouds appear white in the SEVIRI image as they reflect strongly across all three channels, see also EUMETSAT's SEVIRI natural color RGB Quick Guide (EUMETSAT, 2021). In the MODIS image, both cloud types appear white because the selected channels do not exhibit significant absorption differences between ice and liquid water clouds.

The atmospheric data for the simulations of the satellite images consists of a snapshot from a global simulation using the ICOsahedral Non-hydrostatic (ICON) model (Hohenegger et al., 2023) with a 5 km horizontal grid-spacing in combination with ERA5 data for the upper atmosphere. At this grid spacing, ICON can explicitly resolve individual cloud structures. The ICON data was taken from (Kluft, 2023) and regridded to a regular latitude longitude grid of 0.05°. The simulation time is 01/08/2021 12h00 UTC. The surface data is estimated from daily global surface reflectances from the MYD09CMG Version 6.1 product from June to July 2022. All surfaces are assumed to be Lambertian, due to limitations of the ARTS interface to DISORT, see Section 3.4. Whereas Lambertian surface scattering is a reasonable approximation for land surfaces, it is not ideal for ocean surfaces. For ocean surfaces, a wind roughened ocean surface model like Cox and Munk (1954) or Lin et al. (2016) would be more appropriate. A Wind roughened ocean surface model is not yet implemented in ARTS, but it will be added in the future. Gas absorption and molecular scattering are handled as in Section 4.2 except for that only H_2O, O_2, N_2, O_3, and CO_2 are included as

Table 3
Channels and Mapped RGB Color of MODIS and SEVIRI Used for the Simulation of Figure 6

Sensor	Channel	Wavelength [nm]	Mapped RGB color
MODIS	1	645	Red
MODIS	4	555	Green
MODIS	3	469	Blue
SEVIRI	1	635	Blue
SEVIRI	2	810	Green
SEVIRI	3	1,640	Red

Note. RGB mapping of SEVIRI was taken from EUMETSAT (2025).

absorption species. Five different hydrometeor types were included each with its own particle size distribution: cloud liquid water, cloud ice, rain, snow and graupel. Rain and cloud liquid water are assumed as liquid water spheres and the scattering data was taken from the arts-xml-data package (version 2.6.8), see also Section 2. Cloud ice is assumed as hexagonal columns, snow as 10-plate-aggregate and graupel as droxtal from the scattering database of Yang et al. (2013) and Bi and Yang (2017). The scattering database converted to the ARTS single scattering data format is freely available from Zenodo (https://doi.org/10.5281/zenodo.10807525, 19 September 2024). This hydrometeor setup is not intended to be optimal but was chosen to show the capabilities of ARTS for a plausible set of hydrometeors. In the SEVIRI image ice clouds appear in blueish colors due to the strong absorption at 1,640 nm, whereas liquid clouds appear white. In the MODIS image both clouds appear white. As DISORT assumes a plane parallel atmosphere there are no shadows present. Furthermore, it neglects the spherical shape of the earth and overrates the radiation path within the atmosphere for zenith angles close to 90° resulting in too strong extinction.

5.2. All Sky Full Spectrum Fluxes

With the new features, ARTS allows consistent simulation of radiative fluxes across the full spectrum, from the far infrared to the ultraviolet. The same spectroscopic and scattering data, as well as scattering solver, are used throughout the entire spectral range. This allows consistent simulation of the longwave and shortwave parts of the spectrum with identical scattering and spectrospcopic data. Of course, only if the spectroscopic and scattering data cover the full spectrum. Figure 7 shows an example of a full spectrum flux simulation from 10 cm^{-1} to 100,000 cm^{-1}. The simulation setup and atmospheric data is identical to those used for the satellite image simulation in Section 5.1, with the exception that the atmospheric data is sampled at a 1° grid spacing (every 20th grid point in both latitude and longitude) to reduce the computational load. Sampling the data instead of using 1° averages preserves the atmospheric variability, such as the vertical cloud structure. This especially important when calculating global averages. Furthermore, using for example, grid cell averages of the atmosphere as input can result in different global fluxes compared to using the original data, as fluxes are in general a non-linear function of the atmospheric state and for non-linear functions the average of the function is not equal to the function of the average. Of course, using sampled data instead of averaged data appear noisier when plotted on maps but the overall statistics remain consistent with the original data. As in the satellite image simulation, the DISORT solver was employed, but with 10 streams and configured in flux mode rather than radiance mode. The sub solar point is at 18°N and 0°E. As the scattering database of Yang et al. (2013) and Bi and Yang (2017) ranges only down to 100 cm^{-1} and up to 50,000 cm^{-1}, the scattering data was extrapolated down to 10 cm^{-1} and up to 100,000 cm^{-1}.

For the sake of better understanding, we divide the simulation into a longwave part and a shortwave part. In comparison to observations, we can distinguish between longwave and shortwave by the sources and not by a specific wavenumber threshold. Therefore, the longwave simulation considers only thermal emissions from the atmosphere and the surface as sources whereas the shortwave simulation considers only solar radiation as source. Due to linearity of the radiative transfer equation, the resulting longwave and shortwave fluxes can be simply added to get the full spectrum fluxes. As noted in Section 4.1, accurately capturing fluxes does not require resolving every individual spectral line, but rather representing the overall spectral variability. To balance computational efficiency and accuracy, we use 10,000 frequency points for both the longwave and shortwave spectral regions, instead of the 32,768 points used in Section 4.1, since fluxes are now computed globally at 1° grid spacing (64,800 grid points). The longwave region is sampled linearly from 10 to 5,000 cm^{-1}, while the shortwave region is sampled logarithmically from 1,000 to 100,000 cm^{-1}, each with 10,000 frequency points.

Figure 7c shows the simulated instantaneous all sky net flux at the TOA for the identical atmosphere and sun position as in Figure 6. The net flux is defined as the difference of the incoming shortwave and longwave flux (not shown) and the outgoing shortwave and longwave flux (Figures 7a and 7b). The reddish colors indicate where the atmosphere gains energy and the bluish colors show where the atmosphere loses energy. As expected, over the daylight side the atmosphere gains energy and over the night side it loses energy. The whitish areas except for the twilight zone indicate how clouds reduce the absolute value of the net flux. For example, the deep convective clouds over the equator reflect most of the incoming radiation back to space resulting in a strongly reduced net flux. Over the day side clouds reduce the net flux and over the night side clouds increase the net flux. Quantitatively, this is shown in Figure 7d, which shows the cloud radiative effect on the net flux at the TOA. The cloud

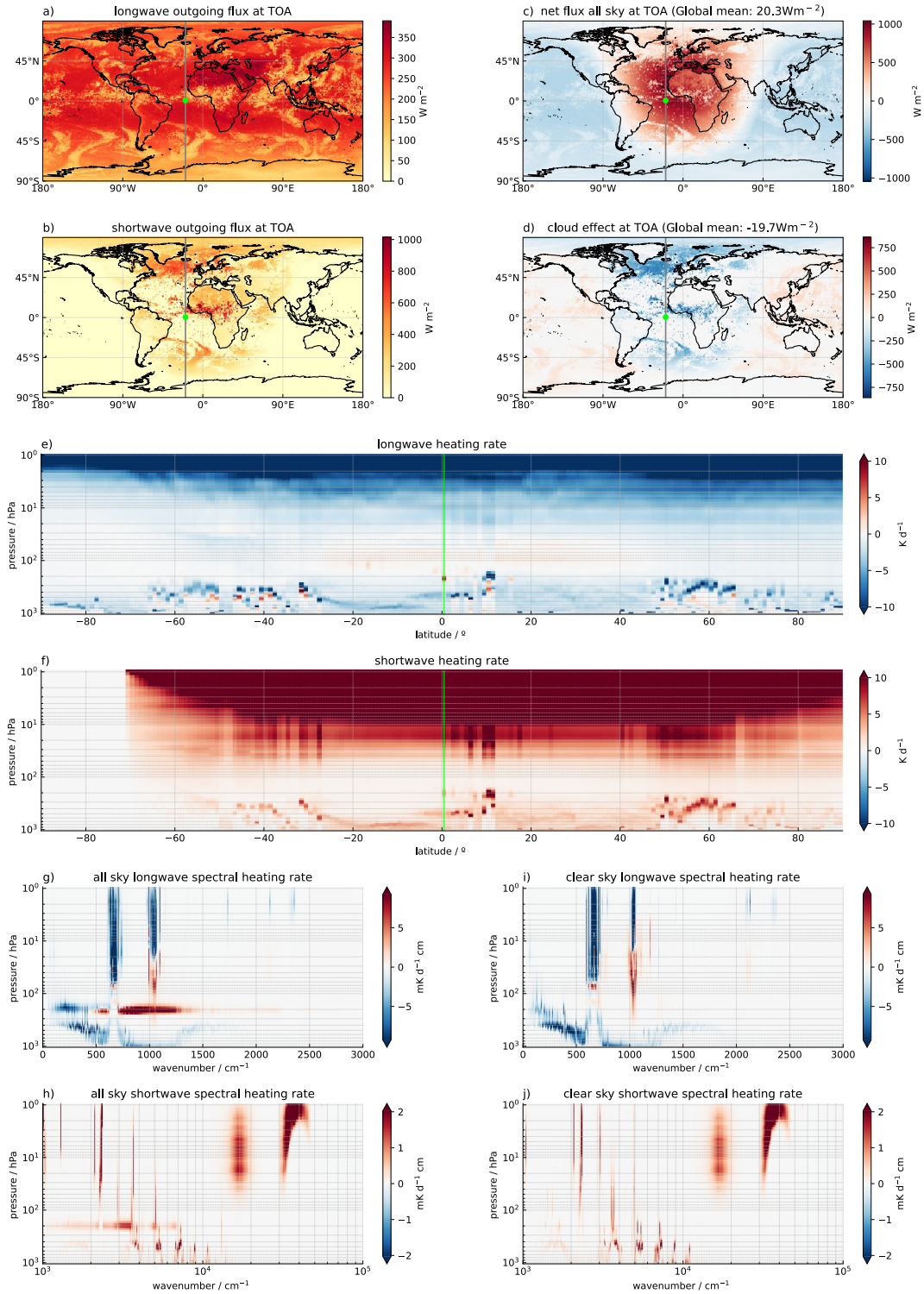

Figure 7. Simulated longwave and shortwave fluxes. See Section 5.2 for details. The gray line in panels (a–d) marks the location of the meridional heating rate cross-section shown in panels (e) and (f). The green line in panels (e) and (f) indicates the position of the spectral heating rate cross-section in panels (g–j). The green dot in panels (a–d) marks the position for the spectral heating rate profiles in panels (g–j).

radiative effect is defined as the difference between the net flux with and without clouds. It is negative over the day side and positive over the night side.

In atmospheric dynamics often not the net flux is of interest but the radiative heating rate H, which indicate where the atmosphere cools or warms due to net emission or net absorption of radiation. Assuming hydrostatic equilibrium it is defined as

$$H = \frac{g}{c_p}\frac{dF_{net}}{dp}, \tag{18}$$

where g is the gravity, c_p is the mass specific heat capacity at constant pressure, F_{net} is the net flux and p is the pressure.

Figures 7e and 7f show separately the longwave and shortwave heating rates along the gray line of Figure 7c as function of latitude and pressure. The reddish colors for the shortwave heating rate indicate that the atmosphere is warmed due to absorption of solar radiation especially at the ozone layer between 1 hPa and 10 hPa and at top of clouds for example, the deep convective system at 5°N. Due to reflection of clouds the shortwave heating rate is even stronger in the stratosphere for all sky conditions than for clear sky conditions. The mostly bluish colors for the longwave heating rate indicate that the atmosphere is cooled by the emission of thermal radiation, where the strongest cooling occurs at the top of the clouds. Warming mostly occurs at the bottom of the clouds or within the stratosphere. Interestingly, there is weakly positive longwave heating rate around 200 hPa at the equator, whereas north and south of it the heating rate is either zero or negative. These kind of positive longwave heating rates are particularly relevant for troposphere-stratosphere exchange Corti et al. (2006); Holton et al. (1995).

Given that ARTS is a line by line model we can investigate the spectral heating rate H_{spc}. It is defined similar to Equation 18 but with the spectral net flux $F_{net,spc}$ instead of the net flux F_{net}. The spectral heating rate shows where which part of the spectrum contributes to the heating or cooling of the atmosphere (Buehler et al., 2006; S. A. Clough et al., 1992). Figures 7g–7j shows separately for shortwave, longwave for all sky and clear sky conditions the spectral heating rate for the green line in Figure 7f and the green dot in Figure 7c. For clear sky conditions, which we simulated by setting all hydrometeors to zero, no heating occurs at 200 hPa either for shortwave or long wave. For all sky conditions, the shortwave heating rate is positive at 200 hPa indicating that there are clouds which absorb solar radiation between 1,000 cm^{-1} and 10,000 cm^{-1}. The long wave heating rate at 200 hPa is negative up to 500 cm^{-1}, but it is positive for between 500 cm^{-1} and 600 cm^{-1} and between 700 cm^{-1} and 1,500 cm^{-1} as seen in Figure 7g. Between 200 cm^{-1} and 500 cm^{-1} the cloud absorbs mostly radiation coming from the middle troposphere which is too small to balance the self emission of the cloud resulting in a negative heating rate. Between 500 cm^{-1} and 600 cm^{-1} and between 700 cm^{-1} and 1,500 cm^{-1} the cloud absorbs mostly radiation coming from the lower troposphere or the surface which is large enough to overcompensate the self emission of the cloud resulting in a positive heating rate. For a more detailed explanation, see Appendix B.

The cloud does not only change the heating at its position and below but also above. The latter is a consequence of the changed upward flux above the cloud. For example, the positive heating rates around the O_3 band at 1,050 cm^{-1} between 100 hPa and 10 hPa as seen in for clear sky conditions is strongly reduced for all sky conditions.

6. Conclusions

We extended ARTS to simulate shortwave radiation by adding a CBS to simulate solar sources. We further add the iyClearsky solver, which support collimated beam sources and solar back ground sources. Additionally, we have updated the DISORT interface in ARTS to shortwave radiation and fluxes.

ARTS and LBLRTM agree well for clear sky fluxes in the RFMIP present day scenario. The RMSD between them is 0.70 Wm^{-2} for the upward flux at TOA and 0.66 Wm^{-2} for the downward flux at the surface. Combined with previous shortwave cross-section applications of ARTS (Emde et al., 2016; Gasteiger et al., 2014) and the use of the established DISORT solver (Buras et al., 2011; Stamnes et al., 2000), this demonstrates that ARTS can simulate accurately shortwave clear sky fluxes and shortwave absorption.

We demonstrated that the new iyClearsky solver can handle limb-viewing geometries, solar occultation, and atmospheric curvature while neglecting multiple scattering and particulate scattering. Neglecting multiple scattering even in clear sky conditions confines iyClearsky to cases with low surface reflectivity and small single scattering albedo. In case of limb viewing geometries, it is further restricted to cases where the line of sight direction is close to the direction of the sun. Because ARTS currently lacks a refractive-index parametrization for the shortwave range, we omitted refraction in the simulation, where we used iyClearsky. Refraction can be important for limb-viewing geometries and solar occultation, particularly when the tangent height is close to the surface, as it affects the apparent position and shape of the solar disc. Given these limitations, iyClearsky is not intended to be a fully developed solver; rather, it provides a starting point for further development, as it already incorporates spherical atmospheric geometry, polarization, collimated beam sources, and a solar background source.

We showed that ARTS can simulate images as seen from geostationary satellites with MODIS- and SEVIRI-like sensors within the limitations of 1D radiative transfer, that is, neglecting shadows and spherical geometry. These simulations demonstrate ARTS' ability to simulate shortwave radiances in cloudy atmospheres using DISORT.

With the newly implemented features ARTS can now simulate radiation from the Microwave to the UV range. This allows to simulate consistent full spectrum fluxes and heating rates, which allows to investigate the interaction of climate and radiation especially the spectral aspect in much more detail.

Given the limitations of the iyClearsky solver, it is clear that the main use cases of ARTS for shortwave simulations will be flux and radiance simulations for 1D plane-parallel atmospheres using the DISORT solver.

For the future, we need to tackle four main issues. First, simulating an ocean surface with specular or Lambertian reflection is not ideal in the shortwave range. Therefore, we need to implement a wind roughened ocean surface model like Cox and Munk (1954) or Lin et al. (2016). Second, we need to implement a more sophisticated Rayleigh scattering cross-section model like the one from Bates (1984) or Tomasi et al. (2005). Third, we need to implement a refractive index parametrization for the shortwave range to account for refraction of solar radiation in the atmosphere. This is important for limb viewing geometries and solar occultation. Fourth, we need to include scattering data and/or parametrizations for aerosols as they are important scatterers within the shortwave range. Despite the issues mentioned above, ARTS is already a powerful and versatile tool for the shortwave range for investigating and simulating the interaction of radiation and atmosphere especially by its line-by-line capability.

Appendix A: Definition of Spectral Radiance and Irradiance

Here we use the definitions similar to Stamnes et al. (2017). The spectral radiance I is defined as the amount of energy dE per time dt, that goes through area dA in direction $\hat{\Omega}$ and within solid angle $d\omega$ per frequency $d\nu$

$$I = \frac{dE}{\cos\theta dA\ dt\ d\omega\ d\nu} \tag{A1}$$

with θ the angle between the normal of the area dA and the direction $\hat{\Omega}$.

The spectral irradiance F or spectral flux is defined as the amount of energy dE per time dt, that goes through area dA per frequency $d\nu$, which can be derived from the spectral radiance multiplied by the cosine of θ by integrating over the solid angle $d\omega$

$$F = \int_{\omega} I \cos\theta\ d\omega. \tag{A2}$$

If the angular integration is confined to the upward hemisphere, the flux is called upward flux F^{+} and if the angular integration is confined to the downward hemisphere, the flux is called downward Flux F^{-}. Adding the upward and downward flux results in the net flux F_{net} which is the same as integrate Equation A2 over the whole sphere.

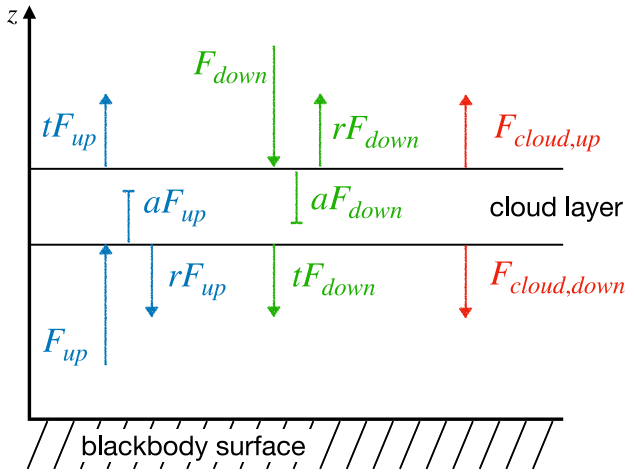

Figure B1. Sketch of a small but high homogenous cloud layer with temperature T over a blackbody surface. rF_i, tF_i and aF_i denote the reflected, the transmitted and absorbed spectral flux and $F_{cloud,i}$ the emitted spectral flux with $i = up, down$.

Appendix B: Explanation for the Spectral Heating Rate of Figure 7g

In this section we give an explanation for the behavior of the longwave all sky spectral heating rate H_{spc} as shown in Figure 7g. Let us assume that we have a typical tropical atmosphere with a small but high homogenous cloud layer with temperature T over a blackbody surface as depicted in Figure B1. From below and above the spectral fluxes F_{up} and F_{down} impact the cloud layer. From energy conservation follows

$$F_i = rF_i + tF_i + aF_i \tag{B1}$$

with $i = up, down$, rF_i the reflected, tF_i transmitted and aF_i absorbed spectral irradiance. For the heating or cooling of the cloud layer, the absorbed spectral flux only is important, because the reflected and transmitted spectral fluxes by definition are not deposited into the cloud layer. The cloud layer emits the spectral fluxes $F_{cloud,up}$ and $F_{cloud,down}$, which are governed by the temperature of the cloud layer and its emission strength.

$$F_{cloud,i} = \epsilon\pi B(T) \tag{B2}$$

with $i = up, down$, $B(T)$ the Planck function at temperature T. For the radiation budget ΔF^* of the cloud layer holds

$$\Delta F^* = aF_{up} + aF_{down} - 2\epsilon\pi B(T) \tag{B3}$$

The absorption strength a and the emission strength ϵ are solely functions of the cloud layer and have in local thermal equilibrium the same numerical value (Kirchhoff's law). This simplifies Equation B3 to

$$\Delta F = (F_{up} + F_{down}) - 2\pi B(T) \tag{B4}$$

This means that the cloud layer heats up if ΔF is positive (absorption > emission) and cools down if ΔF is negative (absorption < emission). As there is not much IR radiation coming from above the cloud at high altitude, we can neglect F_{down} and Equation B4 simplifies to

$$\Delta F = F_{up} - 2\pi B(T) \tag{B5}$$

As there are no clouds underneath the cloud layer, we can rewrite F_{up} as

$$F_{up} = \pi B(T_{em}) \tag{B6}$$

with T_{em} the emission temperature of the atmosphere below the cloud. With Equation B6 and we can translate Equation B5 to

$$\frac{B(T)}{B(T_{em})} < \frac{1}{2} \Rightarrow H > 0 \tag{B7}$$

with H the heating rate. This means that the cloud layer heats up if the absorbed upward going spectral flux is two times higher than the emitted spectral flux and vice versa. If we assume a cloud temperature T of 220 K than the incoming spectral flux between 200 cm^{-1} and 500 cm^{-1} must have emission temperatures >280 K (see Figure B2) to balance the cloud emission. Between 200 cm^{-1} and 500 cm^{-1} the cloud hitting spectral flux typically originates from the middle atmosphere or even from just below the cloud layer. Thus, the temperature difference is too small and the absorbed spectral flux cannot balance the cloud emission, which results in a

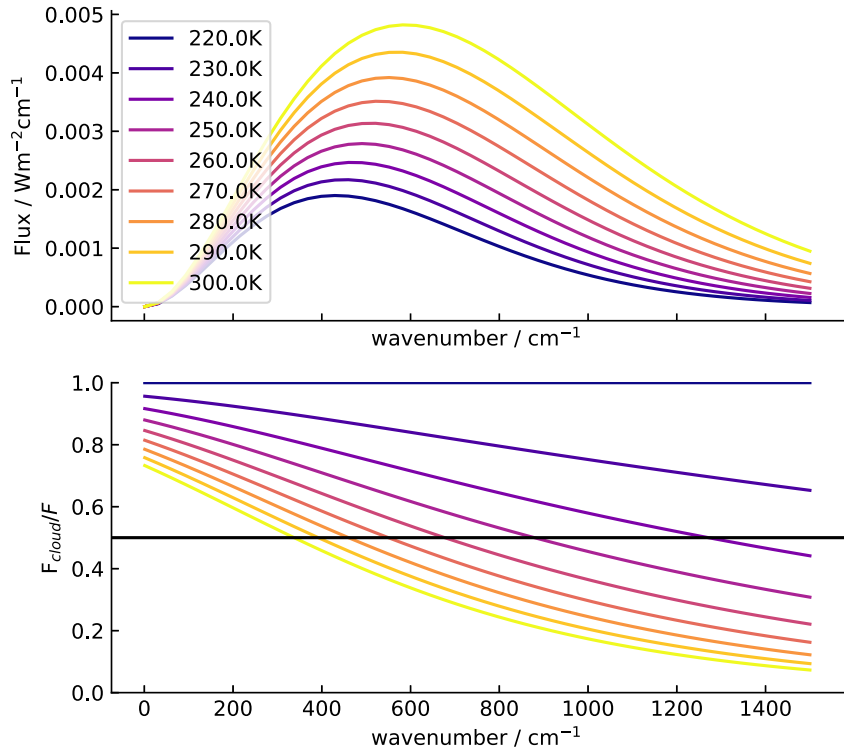

Figure B2. (Top) Spectral flux of a blackbody for different temperatures (bottom) Ratio between spectral flux for different temperatures and the spectral flux for 220 K. It resembles Equation B7 for a cloud temperature of 220 K. The black line indicates if the heating rate is positive or negative. Above the black line the heating rate is negative and below the black line the heating rate is positive. For details see Appendix Appendix (B).

negative heating rate. Above 500 cm^{-1} the needed emission temperatures are <280 K. Between 500 cm^{-1} and 600 cm^{-1} the spectral flux originates from the lower troposphere and between 700 cm^{-1} and 1,500 cm^{-1} additionally also from the surface. The temperature difference is large enough to compensate the cloud emission, which results in a positive heating rate.

Conflict of Interest

The authors declare no conflicts of interest relevant to this study.

Availability Statement

The data and the python scripts for the simulations in this article, if not stated otherwise in the text, are stored on Zenodo (Brath, 2025).

Acknowledgments
The authors would like to thank Lukas Kluft of the Max Planck Institute for Meteorology, Hamburg, Germany, for providing the ICON data. The authors would also like to thank Oliver Lemke and Richard Larsson, both of Universität Hamburg, Germany, for their programming support. For the Hamburg authors, this work is a contribution to the Centrum für Erdsystemforschung und Nachhaltigkeit (CEN). With its capabilities for calculating atmospheric energetics, ARTS also contributes to the Cluster of Excellence "CLICCS — Climate, Climatic Change, and Society". Patrick Eriksson was financially supported by the Swedish National Space Agency (SNSA, Grant 65/18). Last but not, we would like to thank the three anonymous reviewers for their valuable comments, which helped to improve the manuscript. Open access funding enabled and organized by Projekt DEAL.

References

Anderson, G. P., Clough, S. A., Kneizys, F. X., Chetwynd, J. H., & Shettle, E. P. (1986). AFGL atmospheric constituent profiles (0.120km).
Bates, D. (1984). Rayleigh scattering by air. *Planetary and Space Science*, *32*(6), 785–790. https://doi.org/10.1016/0032-0633(84)90102-8
Berk, A., & Hawes, F. (2017). Validation of modtran®6 and its line-by-line algorithm. *Journal of Quantitative Spectroscopy and Radiative Transfer*, *203*, 542–556. https://doi.org/10.1016/j.jqsrt.2017.03.004
Bi, L., & Yang, P. (2017). Improved ice particle optical property simulations in the ultraviolet to far-infrared regime. *Journal of Quantitative Spectroscopy and Radiative Transfer*, *189*, 228–237. https://doi.org/10.1016/j.jqsrt.2016.12.007
Bodhaine, B. A., Wood, N. B., Dutton, E. G., & Slusser, J. R. (1999). On rayleigh optical depth calculations. *Journal of Atmospheric and Oceanic Technology*, *16*(11), 1854–1861. https://doi.org/10.1175/1520-0426(1999)016⟨1854:ORODC⟩2.0.CO;2
Brath, M. (2025). Supplement to "extending the atmospheric radiative transfer simulator (arts) to shortwave radiation" [Dataset]. *Zenodo*. https://doi.org/10.5281/zenodo.16421804
Buehler, S. A., Brath, M., Lemke, O., Hodnebrog, Ø., Pincus, R., Eriksson, P., et al. (2022). A new halocarbon absorption model based on hitran cross-section data and new estimates of halocarbon instantaneous clear-sky radiative forcing. *Journal of Advances in Modeling Earth Systems*, *14*(11), e2022MS003239. https://doi.org/10.1029/2022MS003239

Buehler, S. A., Eriksson, P., Kuhn, T., von Engeln, A., & Verdes, C. (2005). Arts, the atmospheric radiative transfer simulator. *Journal of Quantitative Spectroscopy and Radiative Transfer*, *91*(1), 65–93. https://doi.org/10.1016/j.jqsrt.2004.05.051

Buehler, S. A., Eriksson, P., Lemke, O., Larsson, R., Pfreundschuh, S., & Brath, M. (2024). ARTS - The atmospheric radiative transfer simulator (2.6.8). https://zenodo.org/records/14761537

Buehler, S. A., Larsson, R., Lemke, O., Pfreundschuh, S., Brath, M., Adams, I., et al. (2025). The atmospheric radiative transfer simulator arts, version 2.6 — Deep python integration. *Journal of Quantitative Spectroscopy and Radiative Transfer*, *341*, 109443. https://doi.org/10.1016/j.jqsrt.2025.109443

Buehler, S. A., Mendrok, J., Eriksson, P., Perrin, A., Larsson, R., & Lemke, O. (2018). Arts, the atmospheric radiative transfer simulator – Version 2.2, the planetary toolbox edition. *Geoscientific Model Development*, *11*(4), 1537–1556. https://doi.org/10.5194/gmd-11-1537-2018

Buehler, S. A., von Engeln, A., Brocard, E., John, V., Kuhn, T., & Eriksson, P. (2006). Recent developments in the line-by-line modeling of outgoing longwave radiation. *Journal of Quantitative Spectroscopy and Radiative Transfer*, *98*(3), 446–457. https://doi.org/10.1016/j.jqsrt.2005.11.001

Buras, R., Dowling, T., & Emde, C. (2011). New secondary-scattering correction in disort with increased efficiency for forward scattering. *Journal of Quantitative Spectroscopy and Radiative Transfer*, *112*(12), 2028–2034. https://doi.org/10.1016/j.jqsrt.2011.03.019

Clough, S., Shephard, M., Mlawer, E., Delamere, J., Iacono, M., Cady-Pereira, K., et al. (2005). Atmospheric radiative transfer modeling: A summary of the aer codes. *Journal of Quantitative Spectroscopy and Radiative Transfer*, *91*(2), 233–244. https://doi.org/10.1016/j.jqsrt.2004.05.058

Clough, S. A., Iacono, M. J., & Moncet, J.-L. (1992). Line-by-line calculations of atmospheric fluxes and cooling rates: Application to water vapor. *Journal of Geophysical Research*, *97*(D14), 15761–15785. https://doi.org/10.1029/92JD01419

Coddington, O., Lean, J. L., Lindholm, D., Pilewskie, P., Snow, M., & NOAA CDR Program. (2017). Noaa climate data record (cdr) of solar spectral irradiance (ssi), nrlssi version 2.1 (Tech. Rep.). https://doi.org/10.7289/V53776SW

Corti, T., Luo, B. P., Fu, Q., Vömel, H., & Peter, T. (2006). The impact of cirrus clouds on tropical troposphere-to-stratosphere transport. *Atmospheric Chemistry and Physics*, *6*(9), 2539–2547. https://doi.org/10.5194/acp-6-2539-2006

Cox, C., & Munk, W. (1954). Statistics of the sea surface derived from sun glitter. *Journal of Marine Research*, *13*(2), 814.

Dudhia, A. (2017). The reference forward model (rfm). *Journal of Quantitative Spectroscopy and Radiative Transfer*, *186*, 243–253. (Satellite Remote Sensing and Spectroscopy: Joint ACE-Odin Meeting, October 2015). https://doi.org/10.1016/j.jqsrt.2016.06.018

Eberhard, W. L. (2010). Correct equations and common approximations for calculating rayleigh scatter in pure gases and mixtures and evaluation of differences. *Applied Optics*, *49*(7), 1116–1130. https://doi.org/10.1364/AO.49.001116

Edwards, J. M., & Slingo, A. (1996). Studies with a flexible new radiation code. i: Choosing a configuration for a large-scale model. *Quarterly Journal of the Royal Meteorological Society*, *122*(531), 689–719. https://doi.org/10.1002/qj.49712253107

Emde, C., Buras-Schnell, R., Kylling, A., Mayer, B., Gasteiger, J., Hamann, U., et al. (2016). The libRadtran software package for radiative transfer calculations (version 2.0.1). *Geoscientific Model Development*, *9*(5), 1647–1672. https://doi.org/10.5194/gmd-9-1647-2016

Eriksson, P., Buehler, S., Davis, C., Emde, C., & Lemke, O. (2011). Arts, the atmospheric radiative transfer simulator, version 2. *Journal of Quantitative Spectroscopy and Radiative Transfer*, *112*(10), 1551–1558. https://doi.org/10.1016/j.jqsrt.2011.03.001

EUMETSAT. (2021). Seviri natural colour rgbquick guide. Retrieved 2025-12-17, from Retrieved from https://eumetrain.org/sites/default/files/2021-05/NaturalColoursRGB.pdf

EUMETSAT. (2025). Rgb recipes. Retrieved 2025-07-23, from Retrieved from https://eumetrain.org/sites/default/files/2022-10/RGB_recipes.pdf

Evans, K. F., & Stephens, G. L. (1995). Microwave radiative transfer through clouds composed of realistically shaped ice crystals. Part ii. remote sensing of ice clouds. *Journal of the Atmospheric Sciences*, *52*(11), 2041–2057. https://doi.org/10.1175/1520-0469(1995)052⟨2041:MRTTCC⟩2.0.CO;2

Gasteiger, J., Emde, C., Mayer, B., Buras, R., Buehler, S., & Lemke, O. (2014). Representative wavelengths absorption parameterization applied to satellite channels and spectral bands. *Journal of Quantitative Spectroscopy and Radiative Transfer*, *148*, 99–115. https://doi.org/10.1016/j.jqsrt.2014.06.024

Gordon, I., Rothman, L., Hargreaves, R., Hashemi, R., Karlovets, E., Skinner, F., et al. (2022). The hitran2020 molecular spectroscopic database. *Journal of Quantitative Spectroscopy and Radiative Transfer*, *277*, 107949. https://doi.org/10.1016/j.jqsrt.2021.107949

Gorshelev, V., Serdyuchenko, A., Weber, M., Chehade, W., & Burrows, J. P. (2014). High spectral resolution ozone absorption cross-sections – Part 1: Measurements, data analysis and comparison with previous measurements around 293 k. *Atmospheric Measurement Techniques*, *7*(2), 609–624. https://doi.org/10.5194/amt-7-609-2014

Hansen, J. E., & Travis, L. D. (1974). Light scattering in planetary atmospheres. *Space Science Reviews*, *16*(4), 527–610. https://doi.org/10.1007/BF00168069

Hohenegger, C., Korn, P., Linardakis, L., Redler, R., Schnur, R., Adamidis, P., et al. (2023). Icon-sapphire: Simulating the components of the earth system and their interactions at kilometer and subkilometer scales. *Geoscientific Model Development*, *16*(2), 779–811. https://doi.org/10.5194/gmd-16-779-2023

Holton, J. R., Haynes, P. H., McIntyre, M. E., Douglass, A. R., Rood, R. B., & Pfister, L. (1995). Stratosphere-troposphere exchange. *Reviews of Geophysics*, *33*(4), 403–439. https://doi.org/10.1029/95RG02097

Kluft, L. (2023). Icon monsoon 2.0 ensemble. DOKU at DKRZ. Retrieved from https://hdl.handle.net/21.14106/f8b74dd060c567cb10b56c321add53a3d4618097

Kluft, L., Dacie, S., Brath, M., Buehler, S. A., & Stevens, B. (2021). Temperature-dependence of the clear-sky feedback in radiative-convective equilibrium. *Geophysical Research Letters*, *48*(22), e2021GL094649. https://doi.org/10.1029/2021GL094649

Lafferty, W. J., Solodov, A. M., Weber, A., Olson, W. B., & Hartmann, J.-M. (1996). Infrared collision-induced absorption by n2 near 4.3μm for atmospheric applications: Measurements and empiricalmodeling. *Applied Optics*, *35*(30), 5911–5917. https://doi.org/10.1364/AO.35.005911

Lin, Z., Li, W., Gatebe, C., Poudyal, R., & Stamnes, K. (2016). Radiative transfer simulations of the two-dimensional ocean glint reflectance and determination of the sea surface roughness. *Applied Optics*, *55*(6), 1206–1215. https://doi.org/10.1364/AO.55.001206

Mlawer, E. J., Payne, V. H., Moncet, J.-L., Delamere, J. S., Alvarado, M. J., & Tobin, D. C. (2012). Development and recent evaluation of the mt_ckd model of continuum absorption. Philosophical Transactions of the Royal Society A: Mathematical. *Physical and Engineering Sciences*, *370*(1968), 2520–2556. https://doi.org/10.1098/rsta.2011.0295

Mlawer, E. J., Taubman, S. J., Brown, P. D., Iacono, M. J., & Clough, S. A. (1997). Radiative transfer for inhomogeneous atmospheres: Rrtm, a validated correlated-k model for the longwave. *Journal of Geophysical Research*, *102*(D14), 16663–16682. https://doi.org/10.1029/97JD00237

Oikarinen, L., Sihvola, E., & Kyrölä, E. (1999). Multiple scattering radiance in limb-viewing geometry. *Journal of Geophysical Research*, *104*(D24), 31261–31274. https://doi.org/10.1029/1999JD900969

Paynter, D. J., & Ramaswamy, V. (2011). An assessment of recent water vapor continuum measurements upon longwave and shortwave radiative transfer. *Journal of Geophysical Research*, *116*(D20), D20302. https://doi.org/10.1029/2010JD015505

Penndorf, R. (1957). Tables of the refractive index for standard air and the rayleigh scattering coefficient for the spectral region between 0.2 and 20.0 μ and their application to atmospheric optics. *Journal of the Optical Society of America A: Optics and Image Science*, *47*(2), 176–182. https://doi.org/10.1364/JOSA.47.000176

Pincus, R., Buehler, S. A., Brath, M., Crevoisier, C., Jamil, O., Franklin Evans, K., et al. (2020). Benchmark calculations of radiative forcing by greenhouse gases. *Journal of Geophysical Research: Atmospheres*, *125*(23), e2020JD033483. https://doi.org/10.1029/2020JD033483

Pincus, R., Forster, P. M., & Stevens, B. (2016). The radiative forcing model intercomparison project (rfmip): Experimental protocol for cmip6. *Geoscientific Model Development*, *9*(9), 3447–3460. https://doi.org/10.5194/gmd-9-3447-2016

Serdyuchenko, A., Gorshelev, V., Weber, M., Chehade, W., & Burrows, J. P. (2014). High spectral resolution ozone absorption cross-sections – Part 2: Temperature dependence. *Atmospheric Measurement Techniques*, *7*(2), 625–636. https://doi.org/10.5194/amt-7-625-2014

Stamnes, K., Thomas, G. E., & Stamnes, J. J. (2017). *Radiative transfer in the atmosphere and ocean* (2nd ed.). In (p. 79). Cambridge University Press. https://doi.org/10.1017/9781316148549

Stamnes, K., Tsay, S.-C., Wiscombe, W., & Laszlo, I. (2000). *Disort, a general-purpose fortran program for discrete-ordinate-method radiative transfer in scattering and emitting layered media: Documentation of methodology*. Goddard Space Flight Center, NASA.

Thibault, F., Menoux, V., Doucen, R. L., Rosenmann, L., Hartmann, J.-M., & Boulet, C. (1997). Infrared collision-induced absorption by o2near 6.4 μm for atmospheric applications: Measurements and empiricalmodeling. *Applied Optics*, *36*(3), 563–567. https://doi.org/10.1364/AO.36.000563

Tomasi, C., Vitale, V., Petkov, B., Lupi, A., & Cacciari, A. (2005). Improved algorithm for calculations of rayleigh-scattering optical depth in standard atmospheres. *Applied Optics*, *44*(16), 3320–3341. https://doi.org/10.1364/AO.44.003320

Walker, J. (2017). Colour rendering of spectra. Retrieved 2025-02-13, from https://www.fourmilab.ch/documents/specrend/

Yang, P., Bi, L., Baum, B. A., Liou, K.-N., Kattawar, G. W., Mishchenko, M. I., & Cole, B. (2013). Spectrally consistent scattering, absorption, and polarization properties of atmospheric ice crystals at wavelengths from 0.2 to 100 μm. *Journal of the Atmospheric Sciences*, *70*(1), 330–347. https://doi.org/10.1175/JAS-D-12-039.1

Zawada, D., Franssens, G., Loughman, R., Mikkonen, A., Rozanov, A., Emde, C., et al. (2021). Systematic comparison of vectorial spherical radiative transfer models in limb scattering geometry. *Atmospheric Measurement Techniques*, *14*(5), 3953–3972. https://doi.org/10.5194/amt-14-3953-2021